Probing the in-plane dipole moment vector between ground and excited state of single molecules by the Stark effect

Smit, R.; Ristanovic, Z.; Deperasinska, I. Kozankiewicz, B.; Orrit, M.A.G.J.

ChemPhysChem

Research Article
doi.org/10.1002/cphc.202300881

Chemistry Europe
European Chemical Societies Publishing

www.chemphyschem.org

Probing the in-plane dipole moment vector between ground and excited state of single molecules by the Stark effect

Robert Smit,[a] Zoran Ristanović,[a] Irena Deperasińska,[b] Bolesław Kozankiewicz,[b] and Michel Orrit*[a]

Single molecules, embedded inside a well-defined insertion site of a single-crystalline host matrix, are sensitive probes of electric field via the induced Stark shift on their lifetime-limited electronic transition. Though the response of molecules to electric field has been shown to be relatively homogeneous, crystal symmetry allows for several, spectroscopically-indistinguishable, orientations of the net permanent dipole moment between the ground and excited state – the dipole vector – and this is problematic for measuring field orientation and magnitude. In this work, we measure for each terrylene molecule, embedded inside a new host matrix, the dipole vector independently by an electric field that we can rotate in the plane of the crystal. This single crystal host matrix, called [1]BenzoThieno[3,2-b]BenzoThiophene, induces a moderate symmetry breaking of the embedded centrosymmetric terrylene molecule, and gives rise to a net dipole moment of 0.28 ± 0.09 Debye. Based on quantum chemistry calculations we propose an insertion site that best matches the experimental findings.

1. Introduction

The sensing of electric fields at the nanoscale using molecular probes is a well-studied phenomenon that started with cell membranes[1] and hole-burning experiments.[2] The response of the optical frequency of a single molecule to an electric field manifests itself by means of a linear and/or quadratic shift with field intensity. The linear Stark effect arises from a coupling of the electric field with the difference in static electric dipole moment between the ground and excited state of the single molecule. Likewise, the difference in polarizability tensor between ground and excited state gives rise to a quadratic Stark shift, which usually is much weaker than the linear Stark effect, except when the molecule under consideration is centrosymmetric. Typical fluorescent aromatic molecules used in single-molecule spectroscopy (SMS), e.g. perylene, terrylene, and dibenzoterrylene, have no intrinsic dipole moment due to their centro-symmetry. Hence, to obtain a significant linear Stark shift the molecule either has to be made asymmetric by chemical substitutions,[3] or by insertion into a host crystal that presents a non-centro-symmetric arrangement of host molecules around the guest molecule. Chemical substitutions may lead to unfavourable changes in photophysical properties, such as an increased intersystem crossing rate and/or changes in triplet lifetimes. Another possible consequence of chemical substitutions is an increased electron-phonon coupling, which can negatively influence the strength of the zero-phonon line. A host- or matrix-induced asymmetry has proven to yield the best of both worlds and effectively maintains the photophysical properties of the guest. For dibenzoterrylene (DBT) doped into 2,3-dibromonaphthalene (DBN) crystals it resulted in a linear Stark shift of up to 1.5 GHz/(kV cm^{-1}) at a narrow lifetime-limited linewidth of about 37 MHz.[4] Even higher linear Stark shifts of up to 2 GHz/(kV cm^{-1}) have been observed in semi-crystalline polyethylene doped with terrylene.[5] However, unlike the aforementioned DBT in a DBN crystalline matrix, the linear Stark coefficients in the latter polymer matrix were broadly distributed and the molecules had unstable resonance frequencies.[6] In theory, the sensitivity of molecules to electric field is large enough to detect a single charge at a distance of a few hundred nanometer and could reach the charge sensitivity of single-electron transistors,[7–9] while avoiding complex fabrication techniques. With many molecules as electric field sensors inside a crystal, a charge could in principle be triangulated by mapping its electric field.[7] However, despite narrowly-distributed linear Stark coefficients, the dipole vectors of single molecules can orient in several directions due to symmetry of the insertion site. In the case of DBT in DBN this results for instance in four different in-plane orientations, which are spectroscopically equivalent[4] and typically hard to distinguish with polarized excitation. In order to reliably triangulate single electrons or map electric fields by both direction and magnitude, the specific orientation of each molecule's dipole vector would have to be known. In this work, we examine a method to determine for each molecule the angle and

[a] R. Smit, Z. Ristanović, M. Orrit
Huygens-Kamerlingh Onnes Laboratory, LION, Postbus 9504, 2300 RA Leiden, The Netherlands
E-mail: Orrit@Physics.LeidenUniv.nl

[b] I. Deperasińska, B. Kozankiewicz
Institute of Physics, Polish Academy of Sciences Al. Lotnikow 32/46, 02-668 Warsaw, Poland

Supporting information for this article is available on the WWW under https://doi.org/10.1002/cphc.202300881

magnitude of the dipole vector. Using a quadrupole arrangement of electrodes we vary the direction of a mesoscopic electric field and measure the frequency shift of the molecule. This particular arrangement of electrodes has for instance been applied to defects in SiC[10] or on NV centers.[11] To test this proof of principle on molecular crystals, we performed these experiments on a novel host matrix for single terrylene molecules, namely unsubstituted [1]BenzoThieno[3,2-b]BenzoThiophene, which will be abbreviated as BTBT from now on. We will show that the insertion of terrylene into a BTBT single crystal leads to a relatively strongly broken symmetry, inducing a dipole moment between ground and excited state of terrylene by about 0.28 ± 0.09 Debye. We complement our study by measurements of the spectroscopic and photophysical properties of terrylene in this new host matrix. Furthermore, we determine the orientation of terrylene molecules with polarized excitation and link these studies to quantum chemistry calculations on possible insertion sites for terrylene.

2. Methods

2.1. Crystal preparation and transfer

Procedures of synthesis and purification of BTBT were already described in our recent paper.[12] Single crystals of BTBT doped with terrylene were obtained through co-sublimation in a 0.2 bar argon gas atmosphere at a temperature of about 200 °C, slightly below the melting point of BTBT (217–218 °C). The grown crystals have the form of thin plates of a few tens of μm thick and a surface area of about 10 mm^2. The fragile BTBT crystals were picked up with a sharp glass tip and deposited on the sample. With a small droplet of vacuum grease (Apiezon) it was made certain that the crystals remained in place during the cooldown with liquid helium. Moreover, this insulating layer avoids that charges are injected into the crystal through the electrodes.

2.2. Four-electrode junction preparation

The quadrupole junctions (see Figure S3.3 in the Supporting Information) were patterned by e-beam lithography on a SiO_2-coated (300 nm) p-doped Si wafer (University Wafer) with a spin-coated bi-layer resist (400 nm PMMA 600 kDa and 250 nm PMMA 950 kDa). Both layers were cured for two minutes on a hot plate at 180 °C. After development of the exposed patterns and submersion in a 1:3 MIBK:IPA solution for 30 seconds, the structures were established by evaporating a 5 nm Cr adhesion layer and an 80 nm Au layer. Excess metal was removed by lift-off in heated acetone (45 °C) under continuous stirring. The metal pads were designed to be 0.75 mm apart from the junction area in order to avoid the optical objective from potentially shorting the Al wires (50 μm diameter) that were bonded to 200 μm^2 pads and their connections to the sample holder. The sample holder was connected to two analog outputs of an Adwin Gold DAQ card. The remaining two electrodes were shorted with the ground plane.

2.3. Confocal fluorescence microscopy setup

The measurements were done in a liquid-helium flow cryostat (Janis, SVT-200-5) that can reach a base temperature of 1.2 K. The samples were illuminated through a microscope objective (0.85 NA, Edmund Optics) immersed in the liquid helium, that forms a part of a home-built confocal setup. For the excitation we used a tunable Coherent 699 dye ring laser operated with Rhodamine 6G dye and pumped by a Coherent Verdi V2 laser (5 W at 532 nm). The effective tuning range extended from 560 to 620 nm, while the output wavelength was continuously monitored using a High Finesse WS6-200 wavemeter. Fluorescence was separated from the excitation light by a 615 LP filter and detected by either one or two (for Hanbury-Brown and Twiss experiments) avalanche photodiodes (Excelitas, SPCM-AQRH-16). Fluorescence spectra were recorded with a Horiba iHR320 spectrometer coupled to a liquid-nitrogen-cooled Symphony II CCD detector. Time-correlated single-photon counting was performed using a PicoHarp 300 from PicoQuant. For the start-stop experiments a delay was imposed on the stop channel by a programmable delay box (Ortec DB463). The linear polarization of the excitation beam was controlled with a half-wave plate (Thor Labs, 588 nm zero-order) after cleaning up with a linear polarizer. The polarization state was directly measured using a polarization analyzer (Schäfter + Kirchhoff SK010PA).

3. Results and discussion

3.1. Line-narrowing spectroscopy

BTBT is an elongated aromatic molecule composed of two centro-symmetrically arranged thiophene rings in between two benzene rings (see structure in Figure 1). The origin of the optical absorption of BTBT was measured to be around 367.3 nm and the origin of phosphorescence spectrum was found at 483 nm.[12] Therefore both the singlet and triplet excited states of BTBT are higher in energy than the singlet excited state of terrylene (typically around 580 nm), avoiding quenching of the guest singlet by energy transfer to the host singlet or intermolecular intersystem crossing to the host triplet.[13] A fluorescence spectrum of an ensemble of terrylene molecules in BTBT reveals the existence of at least two spectroscopic sites (Figure 1). Multiple spectroscopic sites are not unusual for terrylene in aromatic host matrices and were for example also found for terrylene in 1,4-dichlorobenzene,[14] anthracene[13] and *p*-terphenyl.[15] The two sites we find are a blue site with origin around 16,869 $cm^{M->1}$ (593.0 nm) and a red site around 16,620 cm^{-1} (601.9 nm). Based on the spectral intensities and the concentration of emitters in our confocal images, the red site appears to have a much higher population than the blue site (Figure S1.1, Supporting Information). In

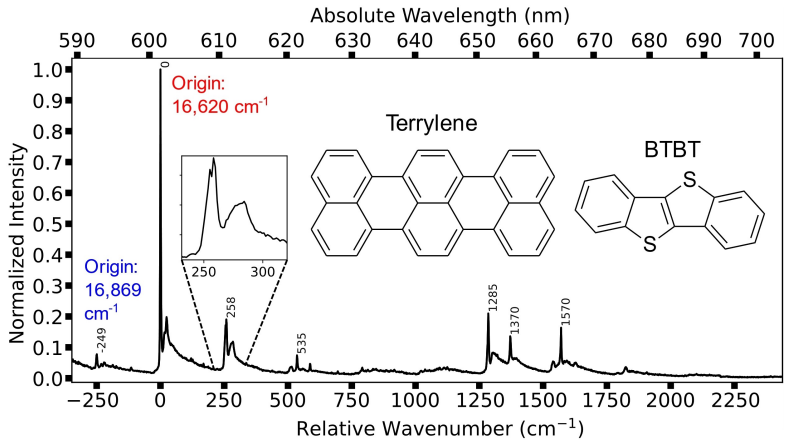

Figure 1. Fluorescence spectrum of an ensemble of terrylene molecules in a BTBT host crystal, excited vibronically with a wavelength of 582.5 nm. The 0–0 ZPL of the red site peaks at 16,620 cm^{-1} (601.9 nm). Note that a feature on the blue side of this line arises from molecules in the blue site: origin at 16,869 cm^{-1} (593.0 nm). The Debye-Waller factor, as the ratio of the intensity of the 0–0 ZPL to the sum of the intensity of the 0–0 ZPL and the phonon side band, is 0.27 ± 0.03. Dominant vibrational peaks are annotated with their frequency position; a more detailed spectrum can be found in Table S1.1 and Figure S1.2 of the Supporting Information. An extensive analysis of the vibrational states of terrylene has been done before.[17]

addition, the blue site is typically characterized by a strong background, which is likely caused by a coincidence of the vibronic line at 258 cm^{-1} of the red site with the 0–0 zero-phonon line (ZPL) of the blue site. This coincidence is noticeable from the fluorescence emission spectrum in Figure 1. The sharp peak is the 0–0 ZPL of the red site, while a weak signal from the blue site is visible around -249 cm^{-1}. The difference in wavenumbers between the two sites is indeed very close to the red site's strong vibronic line around 258 cm^{-1}. Noteworthy is that the red site's spectral position is most red-shifted compared to previous studies of terrylene, where the most red-shifted site was obtained in *para*-dichlorobenzene at 597 nm.[14] Furthermore, the red site's spectrum shows a splitting of the main vibronic line at 255–258 cm^{-1}. Such a splitting could be a signature of non-planar distortion due to insertion in the BTBT crystal, which was similarly observed for terrylene in naphthalene,[16] though with a more pronounced splitting of 13 cm^{-1}. As the red site is the most convenient site to study in terms of background, stability and a high population of terrylene molecules, we will focus mainly on the red site for the rest of the work.

3.2. Photophysical properties

As typically reported for terrylene-doped single-crystal matrices, most terrylene molecules show an excellent spectral stability over longer time.[14,15,18] One example of a spectrally-stable terrylene molecule is given in Figure 2, which shows no spectral diffusion over the measured time of about 20 minutes. Most molecules in the red site are as stable as the molecule in Figure 2, while unstable molecules tend to be more abundant in the blue site. These instabilities are particularly characterized by spectral jumps due to the presence of (tunnelling) two-level systems (Figure S1.4, Supporting Information). Furthermore, spectral diffusion at excitation intensities beyond saturation is

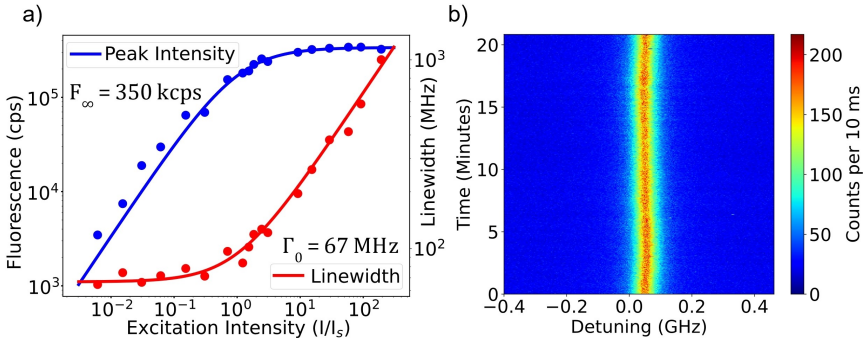

Figure 2. Spectral properties of a single terrylene molecule in the red site. a) Linewidth and fluorescence rate over four orders of magnitude in laser intensity, shown here along with fits of the saturation intensity I_s. The estimated saturation intensity is in the order of 2 W/cm^2. The red data points are the measured linewidths, which are fitted to the broadening equation $\Gamma(I) = \Gamma_0\sqrt{1 + I/I_s}$. The blue data points are the measured fluorescence rates as a function of laser intensity, fitted to $F(I) = F_\infty \frac{I/I_s}{1+I/I_s}$. b) Another molecule followed in real time for more than 20 minutes with an integration time of 10 ms per point.

present in the blue site (Figure S1.5, Supporting Information). This might point to a photo-induced separation of charges in the host crystal.[19]

The homogeneous linewidth for the molecule in Figure 2a is about 67 ± 5 MHz, which is slightly broader than the narrowest linewidths found for terrylene in the red site: about 54 MHz (see distribution of linewidths for the blue and red site in Figure S1.5 in Supporting Information). However, a linewidth of 54 MHz remains broader than what is expected from lifetime-limited terrylene molecules reported in other matrices: ranging from 35 to 45 MHz.[20,21] To determine whether the homogeneous linewidth of 54 MHz is close to the lifetime-limited value, we performed antibunching measurements on single molecules in a Hanbury-Brown-Twiss configuration. We recorded the coincidence histogram of the emitted fluorescence photons with the laser at resonance with the 0–0 ZPL using a 256 ps binning time, while delaying the stop-pulse by 36 ns. As expected, Rabi oscillations appeared at high laser intensities, shown in Figure 3.

Since the detection efficiency of our setup is around 10^{-3}, as determined previously,[23] we can relate the coincidence histograms, for the given time frame, directly to a correlation function.[24] The correlation function for photons can be found by solving the optical Bloch equations with the Laplace transform (see derivation in section 2 of Supporting Information), where we ignored contributions from the triplet state, which only adds photon bunching at longer timescales. The background causes a deviation from zero at the dip and can be taken into account by using the relation: $g_B^{(2)}(\tau) = 1 + \frac{1}{\left(1+B/\langle I\rangle\right)^2}\left(g^{(2)}(\tau) - 1\right)$, where $g_B^{(2)}(\tau)$ is the autocorrelation function that includes background, captured by the term B in relation to the average fluorescence signal $\langle I\rangle$. Finally, the normalized coincidence histograms were fitted to the following correlation function:[20,25]

$$g_B^{(2)}(\tau) = 1 - \frac{1}{\left(1+B/\langle I\rangle\right)^2}\exp\left(-\frac{|\tau|}{2}(\pi\Gamma_0 + \gamma_{21})\right) \times\left[\left(\frac{\pi\Gamma_0 + \gamma_{21}}{2\tilde{\Omega}}\right)\sin(\tilde{\Omega}|\tau|) + \cos(\tilde{\Omega}|\tau|)\right], \quad (1)$$

with $\gamma_{21} = 1/T_1$ being the fluorescence lifetime, $\pi\Gamma_0 = 1/T_2$ the coherence or dephasing time, and $\tilde{\Omega} = \frac{1}{2}\sqrt{4\Omega^2 - \gamma_{21}^2 - (\pi\Gamma_0)^2 + 2\pi\Gamma_0\gamma_{21}}$, where Ω is the Rabi frequency ($\Omega = \left|\vec{\mu}_{12}\vec{E}_{opt}\right|/\hbar$). The slope of the exponential following the dip is given by a sum of parameters that depend on T_1 and T_2, which makes them difficult to separate from the antibunching measurements alone. Hence, we relate T_2 to the homogeneous linewidth $\Gamma_0 = 54$ MHz that we obtained from the excitation spectra through the relation $T_2 = 1/\pi\Gamma_0$. For four molecules we measured and fitted antibunching curves at different excitation intensities, which resulted in an average lifetime $T_1 = 1/\gamma_{21}$ of 3.0 ± 0.2 ns. When calculating the homogeneous linewidth by $\Gamma_0 = 1/2\pi T_1$, the result corresponds to a lifetime-limited linewidth of 53 ± 4 MHz, which indeed corresponds to the smallest linewidths found in this system and shows there is very limited additional dephasing. Nevertheless, this lifetime is on the short side for what was reported for terrylene in other systems, with 3.15 ns being the shortest lifetime measured for terrylene in anthracene.[26] The shorter lifetime for terrylene in anthracene was explained by

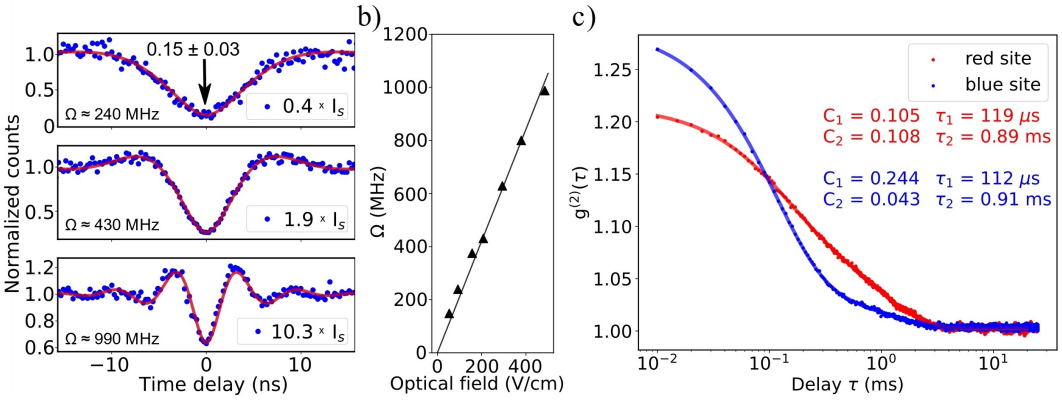

Figure 3. a) Antibunching measurements on a single terrylene molecule at resonance with the 0–0 zero-phonon line, recorded for around 5 minutes per histogram. The three figures correspond to different excitation intensities, as units of the saturation intensity of about 2 W/cm², where the fitted Rabi frequencies are given by Ω. The red curves are fits of the experimental data to equation 1. The data and fit were normalized to approach unity at timescales $\gg T_2$. b) Fitted Rabi frequencies Ω as a function of the estimated optical field intensity at the center of the focused Gaussian beam, using the relation $\Omega = |\mu_{12}||E_{opt}|/\hbar$. The optical field intensities were estimated by $|E_{opt}| = \sqrt{4\eta P/\pi\omega^2}$, with $\eta = \sqrt{\mu_0/\varepsilon_0\varepsilon_r}$ being the wave impedance with $\varepsilon_r \approx 3$, P the laser power corrected for losses and ω the beam waist of about 500 nm. Neglecting an angle between the transition dipole moment μ_{12} and the optical field E_{opt}, the estimated transition dipole moment is about 1 Debye. Later, we will show that the transition dipole moment is estimated to be around 9.4 Debye using quantum chemistry calculations. This could be partly explained by the usual overestimation of the saturation intensity with respect to the true optical field at saturation.[22] c) Fluorescence-autocorrelation functions reveal bunching at the μs to ms time scale due to intersystem crossing (ISC) to the triplet state. The two curves represent data of single molecules in the red and blue sites, taken at about 3 times the saturation intensity. The data was fitted to a bi-exponential decay of the form $g^{(2)}(\tau) = 1 + C_1 e^{-t/\tau_1} + C_2 e^{-t/\tau_2}$, with the obtained parameters for both sites displayed in the image. The fit parameters show a clear difference in contrasts C_1 and C_2, while characteristic time scales for τ_1 and τ_2 are almost equal.

both an enhanced intersystem crossing through the host's triplet and a high refractive index of the anthracene host.[26] Although no report of refractive indices for BTBT can be found, derivatives of BTBT, such as the less-dense polymerized C8-BTBT were reported to have high refractive indices of 1.74 and 1.6 along the out-of-plane and in-plane axes.[27] These refractive indices are relatively close to the refractive indices of anthracene.[28,29] The reduced lifetime of terrylene might therefore be related to a high refractive index of BTBT. In addition, a high refractive index, which can cause a stronger van der Waals interaction with the matrix, might (partly) explain the relative red-shift of the spectroscopic sites in BTBT.

At longer time scales of μs to ms, time-correlated single-photon counting reveals the blinking properties of molecules in the two sites. Fluorescence time traces at resonant excitation were recorded and used for the calculation of the autocorrelation function $g^{(2)}(\tau)$. For molecules in both sites we can distinguish two exponential decays (see Figure 3c) in the autocorrelation, which are assigned to the in-plane T_{xy}-triplet substates for the short decay and the out-of-plane T_z-triplet substate for the long decay.[30,15] For the blue site, the T_z component is relatively weak, which is not the case for the red site. The autocorrelations were recorded at different excitation intensities and processed in a global fit (see Section 2 of the Supporting Information with figures S2.2 till S2.5 showing the fitted data), together with a saturation and linewidth broadening curve such as in Figure 2. The results of the global fit are presented in Table 1. Disregarding inhomogeneity in the ISC rates of single molecules within the sites, the difference among the sites is not that significant. For example, in a pentacene-doped *p*-terphenyl matrix the ISC rates were varying by over two orders of magnitude among spectroscopic sites.[31] However, the triplet lifetimes we find for the two sites are for both the T_{xy}-triplet substates and the T_z-triplet substate about a factor 3 shorter than typically reported for terrylene in other matrices, such as *p*-terphenyl.[15,32] The shorter lifetimes might be the result of a heavy-atom effect and/or distortion of the terrylene molecule in its site.

3.3. Determination of dipole vectors with a 2-D electric field

The coupling of single molecules to an electric field induces shifts of the molecule's energy levels. In first order this gives rise to a linear Stark effect and in second order to a quadratic Stark effect. The linear Stark effect requires a change in the electric dipole moment between ground and excited state, which is a vector: $\Delta\vec{\mu}$. The quadratic Stark effect depends on the change in the polarizability of the molecule between ground and excited state. In the regime of voltages that we applied we observed a moderately strong linear Stark shift with a negligible quadratic component. The dominance of the linear Stark shift is not trivial, as both the BTBT host and terrylene are centrosymmetric. Therefore the change in dipole moment between ground and excited state must be induced by a symmetry-breaking insertion into the host crystal lattice.[4]

We started with typical Stark effect measurements, where a set of parallel electrodes are used to impose an electric field in one dimension. However, the strength of the measured Stark effect depends on the direction of the dipole vector $\Delta\vec{\mu}$ which due to symmetry of the insertion site can have different projections on the imposed electric field. These projections of $\Delta\vec{\mu}$, together with inhomogeneities of $\Delta\vec{\mu}$ from molecule to molecule due to different charge environments, resulted in a complex distribution of the strengths of the Stark shifts that we observed (see Figure S3.2 in the Supporting Information). To reduce this complexity, by measuring the Stark effect independently of the alignment of the crystal to the electrodes, we designed a quadrupole structure with four independently connected electrodes (Figure S3.3 Supporting Information). The crystal is mounted on top of these four electrodes. We apply a bias on the horizontal and vertical electrode pair (Figure 4a). With COMSOL simulations we show that the electric field is mostly homogeneous at the center and moreover we find that the superposition principle of the horizontal and vertical electric field applies, which makes it possible to orient the field in all in-plane directions. These simulations were performed in two dimensions and do not take the substrate or any other anisotropies in the environment into account. Furthermore, the simulations show that the field at the center is a factor 1.2 weaker compared to the naive case where the field is equal to the potential difference divided by the distance between the electrodes (30 μm). This is likely due to concentration of the field between the side tips of the electrodes (see data in Table S3.1 in Supporting Information). The factor of 1.2 was taken into account when fitting experimental data to theory.

As the crystal itself is three-dimensional, the applied electric field is only sensing the projection of $\Delta\vec{\mu}$ in the crystallographic bc-plane, due to the crystalline structure of BTBT.[33] The linear shift of the resonance frequency of the single molecules is given by the scalar product of the two vectors $-\Delta\vec{\mu}.\vec{E}$. Taking into account only the components that are in the plane of the electric field and neglecting crystal anisotropy, the magnitude of the shift reduces to:

Table 1. Spectroscopic and photophysical properties of the blue and red site. The intersystem crossing (ISC) rates and lifetimes of the two distinguishable triplet states, are derived from correlation functions $g^{(2)}(\tau)$, recorded at different excitation intensities. Since these parameters for ISC and triplet lifetimes concern single-molecule measurements they may be affected by the inhomogeneity of the molecules' environment.

Site	Position (cm^{-1})	Narrowest linewidth	ISC rate: γ_{23}^{xy}	Lifetime: γ_{31}^{xy}	ISC rate: γ_{23}^{z}	Lifetime: γ_{31}^{z}
Blue	16,869	43 MHz	$4{,}000 \pm 300\ s^{-1}$	134 ± 3 μs	$170 \pm 50\ s^{-1}$	0.9 ± 0.1 ms
Red	16,620	54 MHz	$1{,}900 \pm 400\ s^{-1}$	125 ± 15 μs	$300 \pm 80\ s^{-1}$	1 ± 0.2 ms

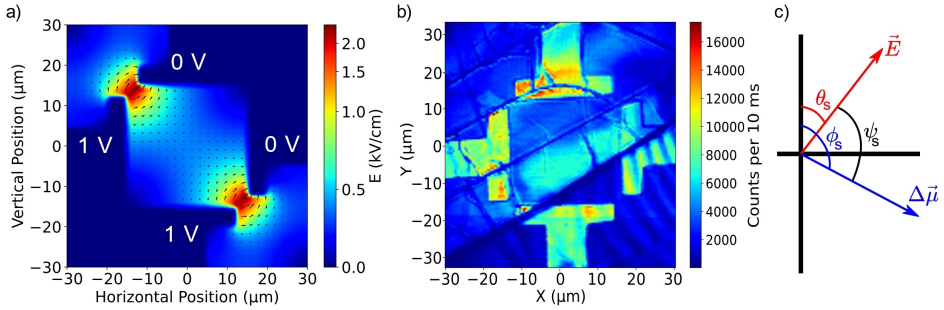

Figure 4. a) COMSOL Simulation of electric field for an isotropic environment with potentials applied to both the bottom electrode (1 V) and left electrode (1 V). The field strength is most homogeneous for an area of approximately 5×5 μm^2 around the center, but changes rapidly further towards the electrodes. Between the side tips of the grounded electrodes and the potentialized electrodes the field is enhanced about six-fold due to the shorter distance. b) Confocal reflection image of the electrodes with a crystal mounted on top. This crystal was used for all measurements in Figures 5 and 6. c) Definitions of the angles used in Figure 5 and 6 and equation 2.

$$\Delta\nu = -|\Delta\vec{\mu}|\left|\vec{E}\right|cos(\psi_s), \quad (2)$$

where ψ_s indicates the angle between the dipole moment $\Delta\vec{\mu}$ and the electric field $\vec{E}$. When we center our frame of reference around the electric field, given by angle θ_s, and defining an angle for the dipole vector, as ϕ_s, the angle ψ_s can be written as $\psi_s = \phi_s - \theta_s$ (see Figure 4c).

With a predefined step size in voltage, all combinations of horizontal and vertical biases are applied within the range of -10 V to 10 V. For each of the combinations we recorded an excitation spectrum around the molecule's 0–0 zero-phonon line (Figure 5a) and fitted this to a Lorentzian distribution to determine its resonance frequency. For all bias combinations, the observed shift of molecule 1 in Figure 5a is plotted in Figure 5b, where the arrows display the electric field direction and magnitude. On the diagonal there is a clear region of white color where little to no shift is observed, even though an electric field is applied. This corresponds to the case where the angle ψ_s is close to 90°. The other diagonal, orthogonal to the white region, represents the direction where the electric field and dipole vector are parallel. On this diagonal, the dipole vector orients in the direction where the Stark shift is negative (equation 2). The orientation found for the dipole of molecule 1 is drawn in Figure 5c. For the three molecules in Figure 5a, the dipole orients in different directions shown by their relationship with field orientation in Figure 5d. Overall, molecule 1 and 3 show good agreement with equation 2, while molecule 2 shows more variation. Moreover, the curve of molecule 2 displays a relatively strong asymmetry between positive (up to $+100$ MHz/kV cm^{-1}) and negative values (down to -150 MHz/kV cm^{-1}). In addition, the curve shows nonlinear behaviour for

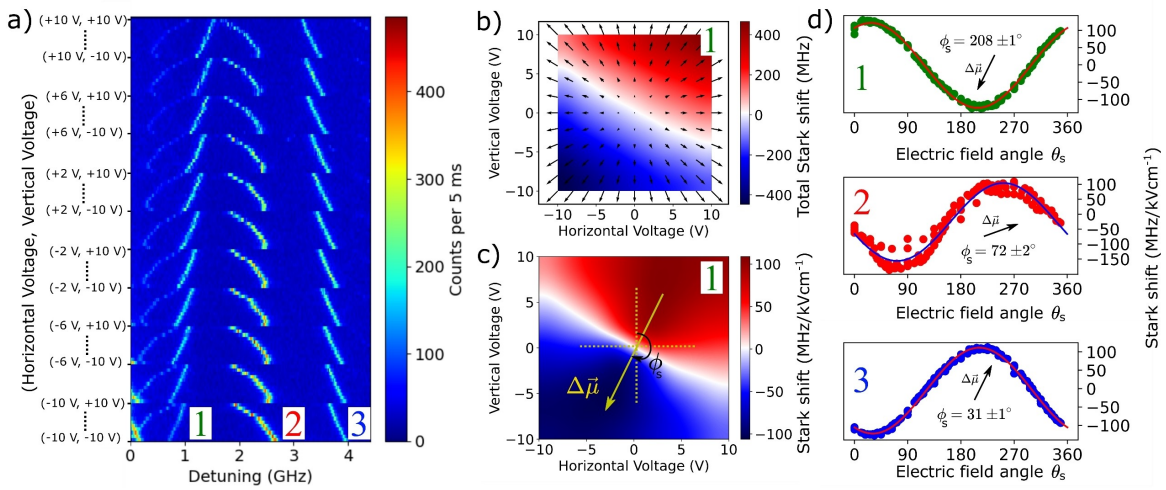

Figure 5. a) Series of 121 single excitation spectra that records the response of molecules in the same focal volume to changing electric field. The scans start with −10 V on both the bottom and left electrode and progresses with a sweep of the voltage on the left electrode from −10 V to 10 V in 11 steps. Subsequently, the voltage on the bottom electrode is increased followed by another sweep of the voltage on the left electrode. Two different patterns can be observed, with molecules moving in both directions. b) Depicts the shift of molecule 1 in (a) for all voltage combinations. The relative magnitude and direction of the applied electric field, in the center between the four electrodes, are plotted as arrows. c) The shifts in (b) are normalized for the magnitude of the electric field vector. The direction of the dipole vector and its angle are plotted in the center. d) The relative magnitude of the Stark effect for the three molecules in (a) is plotted as a function of electric field angle θ_s and fitted to equation 2 as $\frac{\Delta\nu}{|\vec{E}|} = -|\Delta\vec{\mu}|cos(\theta_s - \phi_s)$+offset, where ϕ_s is the angle of the dipole vector $\Delta\vec{\mu}$. The experimental data in (b) and (c) have been smoothed by bicubic interpolation.

sweeps at different voltage combinations, where the electric field vector points roughly in the same direction, but with a different magnitude (different rows in Figure 5b). This may point to an accumulation of charge, which is not observed for molecule 1 and 3. Despite the variations for molecule 2, the angle of the dipole vector can be measured with good accuracy.

To gather statistics on the orientation of the dipole vectors in the red site, we performed the measurements in Figure 5 for a total of 69 molecules. The in-plane position of each molecule was measured, such that the molecules close to the center of the four electrodes could be selected. The Stark coefficient of each molecule is scatter-plotted by its spatial position in Figure 6a. From the plot it becomes clear that outliers, in terms of Stark shift, are indeed further away from the center, where there is either a weak or an enhanced field in the gap between the electrodes (Figure 4a). Closer to the center position, the spread in values is lower and a histogram of the maximum magnitude of the Stark shift, for molecules inside a circle with a radius of 5 μm, reveals a relatively narrow distribution (Figure 5b). The average slope of the Stark shift was measured to be 140 ± 47 MHz/(kV cm^{-1}) and this corresponds to a dipole moment $|\Delta\vec{\mu}|$ of 0.28 ± 0.09 Debye in the bc-plane, which is not corrected for local-field effects around the molecule.[34] The uncertainty of $|\Delta\vec{\mu}|$ can be explained by variations in the electric field further off-center, while also different axial positions of the molecule and charge inhomogeneities around the molecules may contribute to variations of the dipole vector magnitude.

The angle of the dipole moment vector shows a relatively broad distribution (Figure 6c). Although these observations are only for the red site, a broad distribution of angles, possibly due to crystal symmetry, may likewise explain the large variations we observed for the magnitude of the Stark effect with a 1-D electric field for the blue site (Figure S3.2 in the Supporting Information). The distribution for the red site shows that there are at least two populations of molecules, spanning also the opposite quadrant. The drawn dashed lines might be the symmetry axes of the polar distribution. However, the many systems of cracks, possibly also step edges, in Figure 4b made it difficult to relate these lines to crystallographic axes. Nonetheless, the observation of a relatively narrow distribution of linear Stark coefficients, and thus non-random orientations for dipole vectors, points to a symmetry that is broken by the host matrix BTBT. This will set a limit to the possible insertion sites. However, an additional method to determine possible insertion sites is by measuring the direction of the transition dipole moment $\vec{\mu}_{12}$, which follows the long axis of the terrylene molecule, and thus reveals the alignment of the terrylene molecules inside the crystal.

3.4. The transition dipole moment

The transition dipole moment of terrylene, $\vec{\mu}_{12}$, which follows the long axis of the molecule, couples to the optical field $\vec{E}_{opt}$, inducing (Rabi) oscillations between ground and excited state. The coupling between $\vec{\mu}_{12}$ and $\vec{E}_{opt}$ is optimal when the two vectors are parallel. This is achieved by converting the laser light to a linearly-polarized state with a polarizer, while a half-wave plate can tune the angle. As a function of the angle between $\vec{\mu}_{12}$ and $\vec{E}_{opt}$, called ψ_p, the fluorescence intensity varies by a $\cos^2\psi_p$ relationship.

Before we determined the angle of the transition dipole moment for the crystal in Figure 7a, we made sure which crystal cracks represented crystallographic axes, which served as reference axes for $\vec{\mu}_{12}$. To determine the crystallographic axes we illuminated a BTBT single crystal with white light between cross-polarizers. As we rotated the crystal, the crystal turned dark at the four angles where the linearly-polarized light aligned with a crystallographic axis. At in-between angles, the

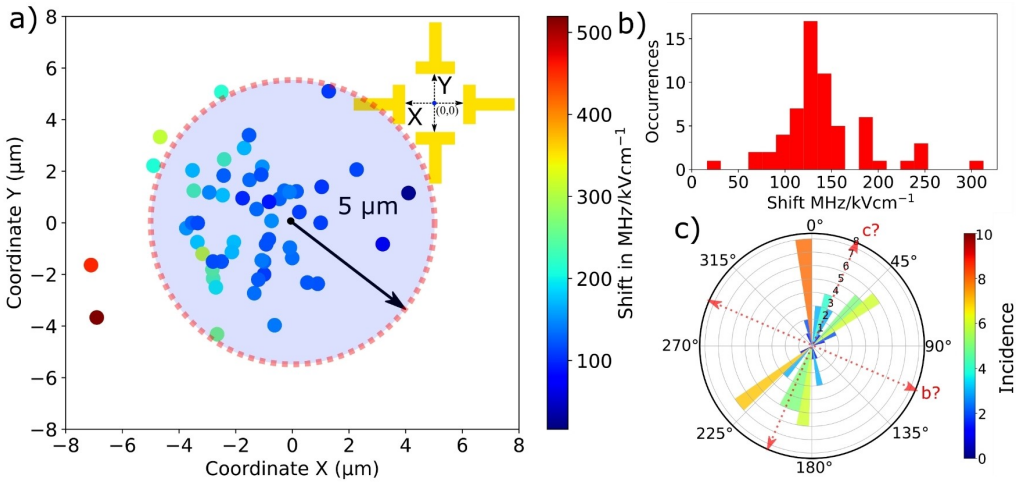

Figure 6. a) Scatter plot of Stark coefficients (maximum shift per unit electric field when the electric field and dipole vector align) for 69 molecules, positioned at their locations with respect to the four electrodes. A circle with radius of 5 μm, drawn from the center between the four electrodes at (0,0), selects the 64 molecules that are closest to the middle and have been plotted in a histogram in b). The distribution of the angles of the dipole vector are plotted in c). Here, the width of the bars indicate the bin size of 9° per bin and both the length and color indicate the number of molecules that are present within each bin. The red dashed arrows indicate possible symmetry axes for the dipole vectors, which based on the insertion sites in section 3.5 could relate to the noted crystallographic axes (bbc insertion site in Table 2).

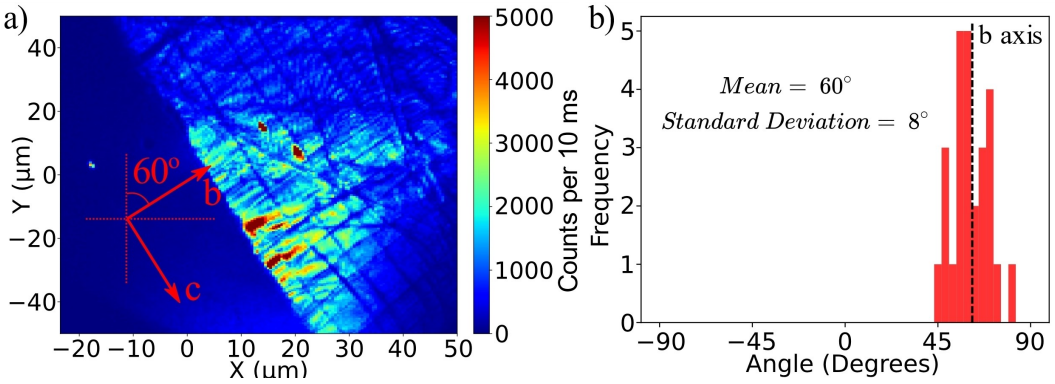

Figure 7. a) Confocal microscope image of a part of a BTBT single crystal. The two red arrows indicate the crystallographic axes as found by cross-polarized illumination. b) Histogram of the transition dipole moment angle with respect to the axes shown in (a) for 26 different molecules. The average angle is around 60° with a standard deviation of 8°. The angle corresponds to the b-axis, which is perpendicular to the crystal edge.

crystal was bright and colourful due to birefringence. The extinction angles coincided with the edge of the crystal and a set of lines perpendicular to the edge, as shown in Figure 7a. However, many lines, of which some of them were possibly step edges, did not coincide with a crystallographic axis.

Single molecules in the red site were excited resonantly by the 0–0 ZPL and their intensity was monitored in the series of excitation spectra, where each line was measured with a different polarization angle (Figure S4.2 in Supporting Information). We changed the polarization of the laser light in a range of 180°, which was sufficient to determine the axis of $\vec{\mu}_{12}$. The intensity of the molecule at various polarization angles is fitted to $I(\theta) = B + A\cos^2(\phi_p - \theta_p)$, where ϕ_p represents the axis of $\vec{\mu}_{12}$, B the background and A the amplitude. This procedure was repeated for 26 molecules and plotted in a histogram in Figure 7b, which shows there is a relatively narrow distribution of transition dipole moments around the b axis, resolved from the outer structure (Figure S4.1, Supporting Information). The same angle of $\vec{\mu}_{12}$ was found at room temperature, where both sites and inhomogeneities have been ensemble averaged (Figure S4.3 in Supporting Information). The similarity of BTBT to anthracene, which crystallizes in the same form, supports an insertion of terrylene along the b-axis.[35] An insertion along the b-axis was found for DBT in anthracene, which apart from the two outer benzene rings closely resembles the shape of terrylene.

3.5. Proposed insertion sites

The equilibrium structure of terrylene inside the BTBT crystal cavities was optimized in the ground (S_0) and excited (S_1) electronic state with Gaussian16[36] using the procedure ONIOM(B3LYP/6-31G(d,p): PM3), i.e. with semiempirical PM3 method describing the rigid crystal structure of BTBT and B3LYP and TD B3LYP/6-31G(d,p) methods for Tr. The cavities inside the BTBT crystal were formed by taking out 2 and 3 BTBT molecules from a crystal element of 48 molecules in a pattern as previously described for DBT in 2,3-dibromonaphthalene[4] and in anthracene crystals.[35] The Franck-Condon factors for $S_0 \rightarrow S_1$ transition were calculated with a procedure included in Gaussian16. The spin-orbit coupling matrix elements between the singlet and triplet states were calculated with ORCA 4.2.1[37] as square root of the sum of squares of spin-orbit coupling matrix elements of all triplet state sublevels of the uncoupled states.

In this paper we continued calculations of the properties of the terrylene molecule in the host crystal structure, using the methods described in our previous papers.[4,35] It relies on the optimization of the structure of the guest molecule embedded in a cavity obtained by removing the appropriate number of host molecules. In the context of the present work our interest was concentrated around the cavities in which terrylene orients with its long axis for the most part parallel to the crystallographic b axis. The three possible sites, called bbb, bbc and bcb', are presented in Figure 8.

In Table 2, the calculations of terrylene in the three sites are shown. We present the calculated (0,0) transition energies, dipole moments in the S_0 and S_1 states and the transition moments. More calculation results are presented in Tables S5.1-3 in the Supporting Information.

The calculated transition energies are slightly smaller than the experimental values. The calculations show that the terrylene molecule loses its planar symmetry. For example, the long axis of the terrylene molecule is slightly longer than twice the distance between BTBT molecules along the b axis, thus a molecule in the cavity bbb is forced to „compensate" this incompatibility by a small deviation from planarity. On the other side, the cavity bbc (Figure 8) forces terrylene to be bent in a bow, which results in a considerably higher dipole moment than in the two other cases.

In view of the results of the calculations, a lack of planar symmetry of terrylene molecule is indicated by the appearance of new vibronic lines, absent in the spectrum of isolated (thus planar) terrylene (see Table S5.1 of the ESI), as well as the appearance of a permanent dipole moment (Table 2 and Table S5.2 of the ESI). Another signature of the symmetry loss are also are the positive (non-zero) elements of the spin-orbit coupling (Table S5.3 of the ESI).

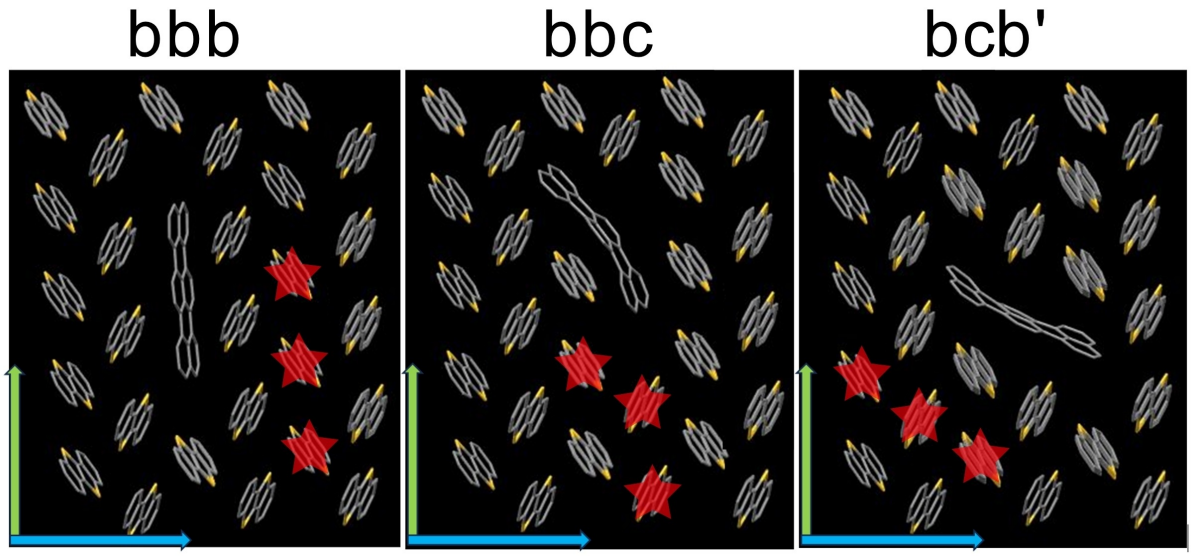

Figure 8. Optimized geometry of terrylene in the three considered cavities, created by the removal of three molecules of BTBT. The red asterisks indicate which molecules have been removed in order to form the cavity for terrylene. The green arrow indicates the b axis and blue the c axis of the BTBT crystal.

Table 2. Results of the ONIOM(B3LYP/6-31G(d,p):PM3) calculation for terrylene embedded in the considered cavities in BTBT crystal. $\lambda(0,0)$ - energy of the (0,0) transition with the zero-point energy correction (more details in Table S5.1 of the Supporting Information), $\mu(S_0 \rightarrow S_1)$, $\mu(S_0)$ and $\mu(S_1)$ are the dipole moments (in Debye) for the $S_0 \rightarrow S_1$ transition, and in the S_0 and S_1 states. Their components are presented along the crystal axes. For isolated terrylene $\lambda(0,0) = 604.3$ nm and $\mu(S_0 \rightarrow S_1) = 9.443$ D. In last rows for the $\mu(S_1) - \mu(S_0)$ we gave, in italic, the results of calculations with use of the simple but uniform B3LYP/3-21G method for the whole system (taken in the geometries optimized by ONIOM).

site		*a-axis*	*b- axis*	*c-axis*	$\lvert\mu\rvert$
bbb	$\mu(S_0 \rightarrow S_1)$	0.274	−9.430	−0.216	9.436
λ (0,0) = 603.7 nm	$\mu(S_0)$	−0.330	−0.108	−0.095	0.360
	$\mu(S_1)$	−0.354	−0.106	−0.102	0.383
	$\mu(S_1) - \mu(S_0)$	−0.024 *(−0.004)*	0.003 *(−0.050)*	−0.007 *(0.001)*	0.023 *(0.050)*
bbc	$\mu(S_0 \rightarrow S_1)$	0.384	8.020	−4.649	9.278
λ(0,0) = 607.1 nm	$\mu(S_0)$	0.456	0.013	−1.756	1.815
	$\mu(S_1)$	0.429	−0.062	−1.648	1.704
	$\mu(S_1) - \mu(S_0)$	−0.027 *(−0.064)*	−0.074 *(−0.102)*	0.108 *(0.182)*	0.111 *(0.218)*
bcb′	$\mu(S_0 \rightarrow S_1)$	−1.642	6.783	6.329	9.422
λ(0,0) = 604.1 nm	$\mu(S_0)$	−0.478	0.303	−0.414	0.701
	$\mu(S_1)$	−0.530	0.301	−0.437	0.750
	$\mu(S_1) - \mu(S_0)$	−0.052 *(0.016)*	−0.002 *(0.001)*	−0.023 *(0.006)*	0.049 *(0.016)*

Out of the three possible cavities occupied by a terrylene molecule, the site bbc seems to be the closest to the experimental red site. Arguments for this assignment are the following:

i) the calculated 0–0 ZPL is most red-shifted (Table 2)

ii) the dipole moment $|\Delta\mu| = \mu(S_1) - \mu(S_0)$ has the highest value, although lower than the experimentally determined 0.28 ± 0.09 D (0.111 D obtained by the ONIOM method, and 0.218 D by using simple B3LYP/3-21G). In addition, the dipole vector has the highest value along the crystallographic axes b and c (Table 2), as suggested from the experiment. The calculated in-plane dipole vector orients about 30° with the c-axis, which indicates that the orientations found for the dipole vectors center around the crystallographic axes drawn in Figure 6c, with possibly four distributions resulting from the four possible, and spectroscopically equivalent, in-plane orientations of the bbc site.

iii) Although the transition dipole moment vector is mostly aligned with the crystallographic b-axis, the bent structure of terrylene creates an angle of about 30° with this axis b.

However, the only possible insertion that follows exactly the b-axis is site bbb, but the centrosymmetric arrangement of host molecules around terrylene in this site would lead to an effective zero dipole moment. The width of the distribution in Figure 7b does not exclude the possibility of a small angle of the transition dipole moment with the b axis.

iv) The highest spin-orbit coupling was calculated for the site bbc.

4. Conclusions

Terrylene molecules embedded in a single crystal of BTBT possess favourable spectroscopic properties in terms of homogeneous linewidths and spectral stability. Furthermore, the studies we performed on the red-most spectroscopic site show that the host matrix induces a broken symmetry of the otherwise centrosymmetric terrylene, giving rise to a net dipole moment of 0.28 ± 0.09 Debye oriented in four in-plane directions. Although the induced net dipole moment could be classified as moderate, when for example compared to dibenzoterrylene (DBT) in 2,3-dibromonapthalene, the magnitude of the dipole vector is still remarkable and might point to a strong influence of the sulphur atoms on the charge distributions in the ground and excited state. For DBT in DBN it was found that mostly the side wings of DBT, which terrylene lacks, were responsible for the induced dipole through the host's bromine atoms.[4] In the case of the BTBT host, the effect of the sulphur atoms on the guest molecule could perhaps be strengthened by replacing terrylene with DBT.

Our reported method on the control of the electric fields' direction, applicable to any crystal, makes it possible to determine the dipole vector for each molecule individually, which would make the use of these molecules for mapping electric fields, by direction and magnitude, or tracing charges, more reliable. In the future, the electric field control could be extended to three dimensions, by using the substrate's p-doped silicon layer as an additional electrode and an ITO cover glass as a top electrode for out-of-plane measurements of the dipole. Moreover, the good hole-conduction properties of BTBT and linear response of molecules to electric field, makes this an interesting system for the study of the injection of charges, for example by a field-effect transistor configuration.[38]

Acknowledgements

We are grateful for the funding provided by NWO (Spinoza prize 2017) that made this work possible.

Conflict of Interests

The authors declare no conflict of interest.

Data Availability Statement

The data that support the findings of this study are available from the corresponding author upon reasonable request.

Keywords: Fluorescence spectroscopy · Single-molecule studies · Stark effect · crystallography · organic semiconductors

[1] H. V. Davila, B. M. Salzberg, L. B. Cohen, A. S. Waggoner, *Nature New Biol.* **1973**, *241*, 159–160.
[2] A. P. Marchetti, M. Scozzafava, R.-H. Young, *Chem. Phys. Lett.* **1977**, *51*, 3.
[3] S. Faez, N. R. Verhart, M. Markoulides, F. Buda, A. Gourdon, M. Orrit, *Faraday Discuss.* **2015**, *184*, 251–262.
[4] A. Moradi, Z. Ristanović, M. Orrit, I. Deperasińska, B. Kozankiewicz, *ChemPhysChem* **2019**, *20*, 55–61.
[5] M. Orrit, J. Bernard, A. Zumbusch, *Chem. Phys. Lett.* **1992**, *196*, 6.
[6] L. Fleury, A. Zumbusch, M. Orrit, R. Brown, J. Bernard, *J. Lumin.* **1993**, *56*, 15–28.
[7] T. Plakhotnik, *ChemPhysChem* **2006**, *7*, 1699–1704.
[8] T. Plakhotnik, *J. Lumin.* **2007**, *127*, 235–238.
[9] S. Faez, S. J. van der Molen, M. Orrit, *Phys. Rev. B* **2014**, *90*, 205405.
[10] M. Rühl, J. Lehmeyer, R. Nagy, M. Weisser, M. Bockstedte, M. Krieger, H. B. Weber, *New J. Phys.* **2021**, *23*, 073002.
[11] L. C. Bassett, F. J. Heremans, C. G. Yale, B. B. Buckley, D. D. Awschalom, *Phys. Rev. Lett.* **2011**, *107*, 266403.
[12] I. Deperasińska, M. Banasiewicz, P. Gawryś, O. Morawski, J. Olas, B. Kozankiewicz, *J. Chem. Phys.* **2021**, *155*, 034504.
[13] A. Nicolet, M. A. Kol'chenko, B. Kozankiewicz, M. Orrit, *J. Chem. Phys.* **2006**, *124*, 164711.
[14] P. Navarro, Y. Tian, M. van Stee, M. Orrit, *ChemPhysChem* **2014**, *15*, 3032–3039.
[15] S. Kummer, Th. Basché, C. Bräuchle, *Chem. Phys. Lett.* **1994**, *229*, 309–316.
[16] I. Deperasińska, B. Kozankiewicz, *Chem. Phys. Lett.* **2017**, *684*, 208–211.
[17] P. Tchénio, A. B. Myers, W. E. Moerner, *Chem. Phys. Lett.* **1993**, *213*, 325–332.
[18] A. A. Gorshelev, A. V. Naumov, I. Yu. Eremchev, Y. G. Vainer, L. Kador, J. Köhler, *ChemPhysChem* **2010**, *11*, 182–187.
[19] M. Colautti, F. S. Piccioli, Z. Ristanović, P. Lombardi, A. Moradi, S. Adhikari, I. Deperasinska, B. Kozankiewicz, M. Orrit, C. Toninelli, *ACS Nano* **2020**, *14*, 13584–13592.
[20] S. Kummer, T. Basche, *J. Phys. Chem.* **1995**, *99*, 17078–17081.
[21] G. S. Harms, T. Irngartinger, D. Reiss, A. Renn, U. P. Wild, *Chem. Phys. Lett.* **1999**, *313*, 533–538.
[22] T. Plakhotnik, W. E. Moerner, V. Palm, U. P. Wild, *Opt. Commun.* **1995**, *114*, 83–88.
[23] R. Smit, Z. Ristanović, B. Kozankiewicz, M. Orrit, *ChemPhysChem* **2022**, *23*, e202100679.
[24] R. Verberk, M. Orrit, *J. Chem. Phys.* **2003**, *119*, 2214–2222.
[25] Th. Basché, W. E. Moerner, M. Orrit, H. Talon, *Phys. Rev. Lett.* **1992**, *69*, 1516–1519.
[26] M. A. Kol'chenko, *Opt. Spectrosc.* **2005**, *98*, 681.
[27] C.-M. Keum, S. Liu, A. Al-Shadeedi, V. Kaphle, M. K. Callens, L. Han, K. Neyts, H. Zhao, M. C. Gather, S. D. Bunge, R. J. Twieg, A. Jakli, B. Lüssem, *Sci. Rep.* **2018**, *8*, 699.
[28] H. C. Wolf, *Z. Naturforsch. A* **1958**, *13*, 414–419.
[29] I. Nakada, *J. Phys. Soc. Jpn.* **1962**, *17*, 113–118.
[30] V. Lawetz, G. Orlandi, W. Siebrand, *J. Chem. Phys.* **1972**, *56*, 4058–4072.
[31] F. G. Patterson, H. W. H. Lee, W. L. Wilson, M. D. Fayer, *Chem. Phys.* **1984**, *84*, 51–60.
[32] A. C. J. Brouwer, E. J. J. Groenen, J. Schmidt, *Phys. Rev. Lett.* **1998**, *80*, 3944–3947.
[33] X. Liu, X. Su, C. Livache, L.-M. Chamoreau, S. Sanaur, L. Sosa-Vargas, J.-C. Ribierre, D. Kreher, E. Lhuillier, E. Lacaze, F. Mathevet, *Org. Electron.* **2020**, *78*, 105605.
[34] A. Aubret, M. Orrit, F. Kulzer, *ChemPhysChem* **2019**, *20*, 345–355.
[35] A. A. L. Nicolet, P. Bordat, C. Hofmann, M. A. Kol'chenko, B. Kozankiewicz, R. Brown, M. Orrit, *ChemPhysChem* **2007**, *8*, 1929–1936.
[36] Gaussian 16, Revision C.01, M. J. Frisch, G. W. Trucks, H. B. Schlegel, G. E. Scuseria, M. A. Robb, J. R. Cheeseman, G. Scalmani, V. Barone, G. A. Petersson, H. Nakatsuji, X. Li, M. Caricato, A. V. Marenich, J. Bloino, B. G. Janesko, R. Gomperts, B. Mennucci, H. P. Hratchian, J. V. Ortiz, A. F.

Izmaylov, J. L. Sonnenberg, Williams, F. Ding, F. Lipparini, F. Egidi, J. Goings, B. Peng, A. Petrone, T. Henderson, D. Ranasinghe, V. G. Zakrzewski, J. Gao, N. Rega, G. Zheng, W. Liang, M. Hada, M. Ehara, K. Toyota, R. Fukuda, J. Hasegawa, M. Ishida, T. Nakajima, Y. Honda, O. Kitao, H. Nakai, T. Vreven, K. Throssell, J. A. Montgomery Jr., J. E. Peralta, F. Ogliaro, M. J. Bearpark, J. J. Heyd, E. N. Brothers, K. N. Kudin, V. N. Staroverov, T. A. Keith, R. Kobayashi, J. Normand, K. Raghavachari, A. P. Rendell, J. C. Burant, S. S. Iyengar, J. Tomasi, M. Cossi, J. M. Millam, M. Klene, C. Adamo, R. Cammi, J. W. Ochterski, R. L. Martin, K. Morokuma, O. Farkas, J. B. Foresman, D. J. Fox, **2016**.

[37] F. Neese, *WIREs Comput. Mol. Sci.* **2018**, *8*, e1327.
[38] A. A. L. Nicolet, M. A. Kol'chenko, C. Hofmann, B. Kozankiewicz, M. Orrit, *Phys. Chem. Chem. Phys.* **2013**, *15*, 4415–4421.

Manuscript received: November 17, 2023
Revised manuscript received: December 22, 2023
Accepted manuscript online: January 11, 2024
Version of record online: January 22, 2024